# Seeing Around Obstacles Using Active Terahertz Imaging

Yiran Cui no and Georgios C. Trichopoulos no, Member, IEEE

Abstract—In this article, we show how active terahertz (THz) imaging systems can exploit the unique propagation properties of THz waves to reconstruct images of nonline-of-sight (NLoS) scenes. Most building surfaces' material properties and roughness allow for a unique combination of diffuse and strong specular scattering. As a result, most surfaces behave as lossy mirrors that enable propagation paths between a THz camera and the NLoS scenes. We propose a mirror folding algorithm that tracks the multireflection propagation of THz waves to correct the image from cluttering and see around occlusions without prior knowledge of the scene geometry and material properties. To validate the feasibility of the proposed NLoS imaging approach, we carried out a numerical analysis and developed two THz imaging systems to demonstrate real-world NLoS imaging experiments in sub-THz bands (270-300 GHz). The results show the capability of THz radar imaging systems to recover both the geometry and pose of LoS and NLoS objects with centimeter-scale resolution in various multipath propagation scenarios. THz NLoS imaging can operate in low visibility conditions (e.g., night, strong ambient light, and smoke) and uses computationally inexpensive image reconstruction algorithms.

*Index Terms*—Active imaging, around-the-corner, nonline-of-sight (NLoS), terahertz (THz).

#### I. INTRODUCTION

DUE to the opaqueness of most materials in the visible and infrared portion of the electromagnetic (EM) spectrum, human vision, as well as regular optical cameras, are capable of seeing objects that are in the direct line-of-sight (LoS). However, when opaque surfaces are present in the scene, occluded objects are not visible. On the other hand, lower frequency EM waves can penetrate most non-metallic or low-loss materials and hence can reveal the anatomy and pose of nonline-of-sight (NLoS) objects and scenes. For example, through-the-wall-radars can detect the presence of humans or discern large objects behind concrete walls or other materials that are opaque in the visible spectrum [1], [2], [3]. Additionally, microwave frequencies have been used to detect NLoS objects through multireflection of the signals on surrounding opaque walls [4], [5], [6]. Nevertheless,

Manuscript received 18 November 2023; revised 18 April 2024; accepted 29 April 2024. Date of publication 14 May 2024; date of current version 5 July 2024. This work was supported by the National Science Foundation under Grant CAREER ECCS-1847138. (Corresponding author: Yiran Cui.)

The authors are with the School of Electrical, Computer and Energy Engineering, Arizona State University, Tempe, AZ 85281 USA (e-mail: ycui36@asu.edu; gtrichop@asu.edu).

Color versions of one or more figures in this article are available at https://doi.org/10.1109/TTHZ.2024.3401041.

Digital Object Identifier 10.1109/TTHZ.2024.3401041

the large wavelength of the low-frequency signals and the limited bandwidth (typically <6 GHz) merely enable detection and tracking rather than clear images with detailed information. Additionally, the transparency of most materials, the small roughness of most surfaces with respect to the wavelength, and edge diffraction result in strong multipath propagation that clutters the reconstructed images. Therefore, microwave NLoS systems can be very effective for sensing hidden objects but offer limited imaging capabilities.

At infrared and optical frequencies, most materials are opaque and surfaces scatter most of the incident waves. As such, an alternative approach to NLoS imaging has been developed by exploiting the multipath propagation of lights, as first introduced in [7] where the authors demonstrate imaging of an occluded object by light scattering via a white, near-Lambertian surface. The method uses a laser for illumination and an ultrafast infrared camera to record the time-of-flight (ToF) of photons, and then images are reconstructed using a filtered back projection-based algorithm. Gariepy et al. showed a simpler approach to detecting NLoS objects [8] and O'Toole et al. [9] demonstrated a confocal NLoS imaging approach that can extend the visible distance; however, it mainly relies on the use of retroreflective surfaces. Liu et al. [10] developed a virtual cameral concept to reduce image reconstruction complexity and account for scenes with multiple diffuse reflections. Despite some other recent advances showing that high-resolution (millimeter-scale [11]), fast-rate (up to 5 fps [12]), multireflection (around two corners []), and long-range (stand-off distance >1.4 km [14]) imaging can be achieved, optical NLoS systems need to contend with several severe challenges.

First, intrinsically, visible lights barely propagate in low visibility conditions such as dust, smoke, fog, and heavy rain. Thus, optical imaging systems tend to fail in these cases. Additionally, optical NLoS imaging inevitably suffers from intense losses due to both free-path propagation and wave scattering on the LoS surfaces [15]. This situation becomes worse when imaging at larger distances or in the presence of ambient light which adds more noise/interference to the receiver. Furthermore, the efficiency of the optical NLoS imaging system greatly relies on high-reflectance surfaces of the LoS surfaces. To alleviate these challenges, expensive and complex hardware with extremely high sensitivity and SNR is required, such as single-photon avalanche diodes and streak cameras. Correspondingly, the use of high-precision optical instruments: could result in noisy measurements when mechanical vibrations are present; may lead to high costs on maintenance and transportation; and may require

 $2156\text{-}342X @ 2024 \ IEEE.\ Personal\ use\ is\ permitted,\ but\ republication/redistribution\ requires\ IEEE\ permission.$  See https://www.ieee.org/publications/rights/index.html for more information.

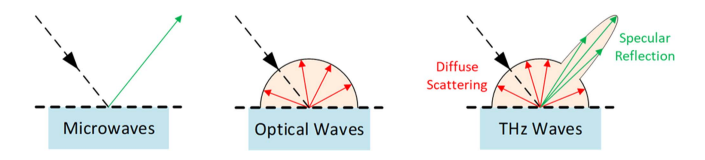


Fig. 1. Wave scattering mechanisms across the EM spectrum.

computationally intensive processing methods to reconstruct images from diffuse scattering.

Besides the optical regime, acoustic waves can also be used to image NLoS scenes [16]. However, acoustic methods: exhibit limited spatial resolution due to the long wavelengths (ultrasound suffers from a short propagation range in free space); are sensitive to ambient sounds; and lack the capability of distinguishing multiple reflections similar to optical systems.

As an emerging technology, the terahertz (THz) spectrum (0.3-3 THz) offers unique wave propagation phenomena that can alleviate many shortcomings of current NLoS imaging approaches. As illustrated in Fig. 1, at lower frequencies (<70 GHz) most building surfaces are smooth compared to the wavelength with negligible diffuse scattering. On the other hand, as previous works have shown, many surfaces can be characterized as near-Lambertian such that diffuse scattering dominates the wave reflection in the optical range. However, in the THz regime, the roughness of most building surfaces is comparable to the wavelength such that wave reflection is characterized by strong specular components as well as diffuse scattering [17]. The specular reflection can be used to establish a strong signal propagation path between the imaging aperture and the NLoS scene. A prior work [18] has exploited the specular reflection to produce images of NLoS objects using a passive THz imaging system. However, the passive approach; requires a prior knowledge of the reflective wall to reveal the NLoS objects' location since the range information cannot be determined in this approach and suffers from weak signals and hence is typically limited to a single bounce and very short distances due to the scattering and propagation losses, respectively. On other hand, active THz imaging systems can generate three-dimensional (3-D) images by recovering the range information of the scene. In this case, diffuse scattering plays a key role in the THz band and can provide critical information on the propagation path of the signals by: revealing the location and orientation (pose) of the surrounding surfaces without a prior knowledge of the geometry and recovers the shape of the objects of interest in the NLoS scene. In a prior work, we have shown a basic imaging setup with a point scatterer for short distance NLoS imaging [19]. Here, we extend the work to include longer imaging distances, multiple bounces, and a NLoS image recovery process that does not require computationally demanding inverse reconstruction algorithms typically used in NLoS imaging [7].

The advances in semiconductor technology and nanofabrication techniques have enabled a plethora of THz active imaging systems that can generate high-resolution 2-D and 3-D images. Such systems include real-time THz cameras [20], stand-off raster scanners [21], as well as multiple-input-multiple-output (MIMO) imaging radars [22]. These systems can use

moderate-sized apertures to generate centimeter-scale resolution images at a > 20-m distance. So far, THz imaging research has focused on astronomy, imaging in low visibility conditions, spectroscopy, and seeing through light clothing for contrabands and security. Extending the vision to the NLoS and seeing around obstacles with THz waves can benefit multiple applications such as first response and rescue missions, detection for hidden traffic/pedestrians, and autonomous navigation. Besides, NLoS THz imaging can take advantage of the expected co-existence of radar and communication systems to provide high-resolution simultaneous localization and mapping for future wireless communication systems [23].

In this article, we present an image reconstruction method that can be applied to multireflection NLoS imaging (*mirror folding*). The method is evaluated first using a set of computationally generated 2-D radar images. Then, we present the measurement results of several experiments in real-life scenarios to further demonstrate the feasibility of THz NLoS imaging. The experiments validate several unique advantages of the proposed THz approach.

- The small wavelengths of THz signals (< 1 mm) and wide bandwidth enable high-accuracy 3-D NLoS imaging with a centimeter-scale resolution.
- 2) The strong specular reflection on the LoS surface allows for a low signal loss, thus images with higher SNR. Using a single THz transceiver with  $\sim$ 50 dB of dynamic range, we accomplished a total imaging range of several meters.
- 3) The THz NLoS imaging reveals not only the hidden targets in the NLoS scenes but also all the reflective surfaces (i.e., mirrors) along the propagation path. As a result, using the proposed *mirror folding* method, a complete image of both LoS and NLoS scenes can be acquired without any prior knowledge, leading to an accurate localization of the invisible targets even when multiple reflections are present.

#### II. THZ RADAR IMAGING AND MIRROR FOLDING

Without loss of generality, we consider active THz imaging systems that generate narrow beams to scan a wide field of view (FoV) and use a finite bandwidth signal to acquire the range information of the backscattered signals (e.g., pulsed or continuous wave systems). The proposed method can also be applied to THz images acquired by alternative systems, including MIMO-based imagers [22], programmable metasurfaces [24], or compressive sensing [25].

### A. Raw Image Generation

To image the invisible scene behind an opaque occlusion, an imaging aperture (THz camera) forms narrow transmitting and receiving beams that illuminate and record the backscattered signals from a LoS surface, respectively. Assuming the LoS surface is a common indoor building material, wave scattering features both strong specular reflection (green arrows) and detectable diffuse scattering that is almost omnidirectional (blue arrows). The latter enables imaging of flat or lightly curved surfaces that are not normal to the imaging system's beam direction. On the

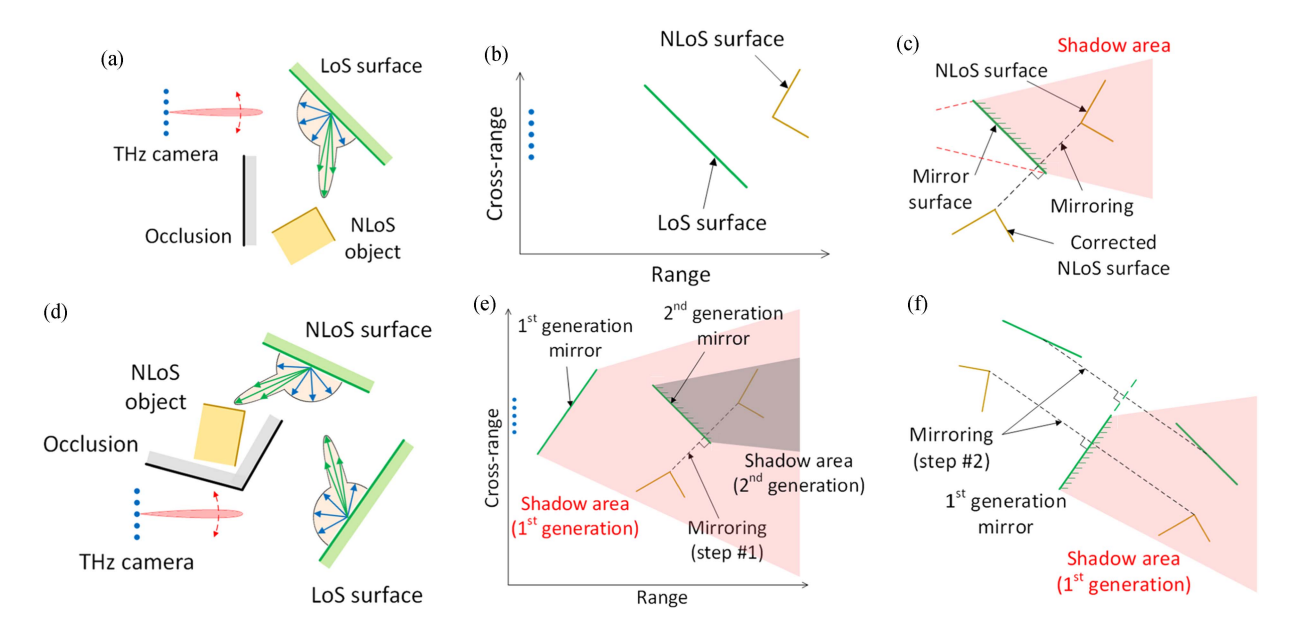


Fig. 2. Mirror folding for reconstruction of NLoS scenes. (a) Illustration of a THz NLoS imaging scenario. Surrounding surfaces are used as mirrors to image the hidden scene behind nontransparent occlusions. (b) Due to the strong specular reflection from the LoS surface, the NLoS object appears as a "ghost" with a wrong pose in the initial image. (c) Assuming the LoS surface behaves as a mirror, the NLoS pose is corrected using *mirror folding*. (d) When multiple reflections between the LoS and NLoS objects are involved, more than one "ghost" objects appear in the initial image. (e) and (f) In this case, *mirror folding* is performed multiple times successively to properly determine the correct geometries.

other hand, the specular reflection allows a relatively low-loss roundtrip path between the aperture and the NLoS area and hence enables seeing around occlusions. In other words, the surrounding surfaces can act as *lossy mirrors* in the THz band and allow a relatively simple image reconstruction algorithm of NloS scenes.

We assume an active imaging system where a narrow beam is scanned in both azimuth and elevation angles to obtain the angle-of-arrival of the backscattered signals. In the meantime, at each scanning angle, the aperture measures the ToF information of the received signals. By combining them, a 3-D image (range and cross-range) of the imaging scene is formed where the value of every voxel corresponds to the intensity of the backscattered signal. We note that: based on the Rayleigh criterion, the angular resolution is  $\theta=1.22\lambda/D$ , where  $\lambda$  and D are the wavelength and aperture diameter, respectively; and according to the sampling theorem, the range resolution is  $c_0/(2B)$ , where  $c_0$  and B are the speed of light in free space and measurement bandwidth, respectively.

Besides, since this article is mainly focused on the principle of THz NLoS imaging, the image reconstruction algorithm does not affect the validity of the proposed approach. Different algorithms can be selected based on the imaging hardware and detailed requirements of computational speed and accuracy. Nevertheless, as a reference, the specific algorithms we used in this article are documented in the Appendix.

#### B. Image Correction Using Mirror Folding

However, due to the nature of THz signal propagation, the 3-D image may comprise backscattered signals originating from both single reflections (i.e., camera  $\rightarrow$  LoS object  $\rightarrow$  camera) and multiple reflections (e.g., camera  $\rightarrow$  LoS object  $\rightarrow$  NLoS

object  $\rightarrow$  LoS object  $\rightarrow$  camera), as illustrated in Fig. 2(a). As a result, although LoS objects can be imaged properly, due to longer propagation paths, signals from NLoS scenes arrive later and appear behind LoS objects with the wrong *pose* (location and orientation) in the initial image, as depicted in Fig. 2(b). This is also known in radars as cluttering and results in a false representation of the scene's geometry.

To correct the NLoS geometries and achieve an accurate image, we assume that, at THz frequencies: all surfaces are opaque and the specular reflection dominates the surface wave scattering. With these assumptions, most building surfaces can be treated as lossy mirrors with the amount of loss depending on the surface roughness and the material properties. This way, the whole area behind a LoS surface (determined by the relative position to the THz camera) is characterized as a "shadow area" [as illustrated in Fig. 2(c)]. Correspondingly, the presence of any object inside this shadow area, classified as "ghost objects", is the result of a secondary reflection.

To account for this propagation, we mirror the objects inside the shadow area around the plane defined by the LoS surface (i.e., mirror) and obtain an image that depicts the NLoS objects with the correct geometries and poses, as shown in Fig. 2(c). We term this operation as *mirror folding* since it reverses the process of mirror unfolding [26]. This method is also computationally efficient as it acts directly on the voxels of the image, thus adding a small overhead to the overall imaging process. On the contrary, in optical NLoS imaging approaches, the large amount of data being processed, and the complex algorithms lead to computationally intensive image reconstructions. For example, the back-projection method can take hours to produce images [7], [27].

Since this method particularly accounts for the objects inside the shadow area, if a NLoS target is only partially in this area,

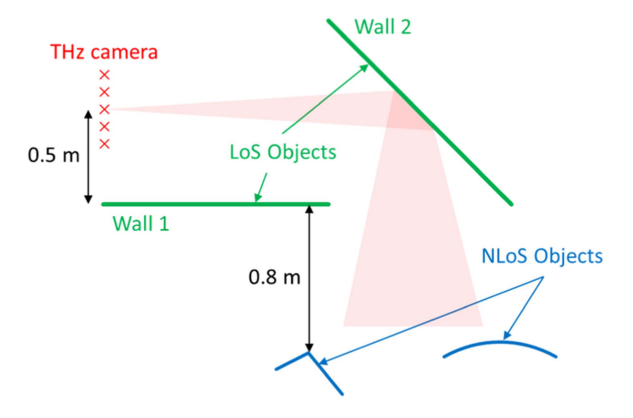


Fig. 3. 2-D geometry of an NLoS imaging scenario. The complex geometry results in multireflection propagation and image cluttering.

it cannot be fully revealed. In this case, we can either increase the imaging FoV or adjust the beam scanning area to cover the entire NLoS target.

Nevertheless, high permittivity and/or high conductivity surfaces can allow multiple wave reflections within the scene of interest. Such propagation, as illustrated in the example of Fig. 2(d), provides an opportunity to extend NLoS imaging to larger scenes but also can result in additional cluttering of the image. We need to perform mirror folding multiple times to obtain the correct image. As depicted in Fig. 2(e) and (f), both the LoS and NLoS surfaces behave as mirrors in the initial image. To facilitate the multistep reconstruction process, we classify the hidden mirrors and objects depending on the number of bounces needed to image them. As such, the hidden mirror in this example is classified as a child mirror to the LoS wall and the object as children to the hidden mirror. Then, mirror folding is first applied to the children objects of the "youngest" mirror and then repeated for the LoS mirror. This hierarchical reconstruction process can be generalized for an arbitrary number of bounces and is discussed in more detail in the Appendix.

# III. SIMULATIONS OF THZ NLOS IMAGING

Simulating an NLoS imaging scenario with a full-wave model is computationally expensive in the THz bands due to electrically large dimensions. For example, one meter corresponds to 1000  $\lambda$  at 300 GHz ( $\lambda$  is the wavelength), and we would need models that have a total surface area of multiple square meters. Thus, computing the field propagation in most THz NLoS scenarios becomes prohibitively demanding in terms of CPU and RAM resources. An alternative approach is to reduce 3-D geometries that are uniform in one dimension (e.g., height) to a 2-D space [28]. For example, a circle in 2-D corresponds to an infinitely long cylinder in 3-D.

We assume a 2-D imaging problem with both LoS and NLoS scenes and a THz camera, as depicted in Fig. 3. In this example, the scene comprises two LoS walls (both are 1 m long) and two NLoS targets (a corner with a total length of 40 cm and a 50 cm-long arc). Wall 1 blocks the direct LoS between the THz camera and the NLoS targets, thus wall 2 is used to image the hidden scene.

To allow the calculation of EM fields on an electrically large model, as the one encountered in a typical indoor propagation scenario, we limit the analysis to a 2-D space (assume objects are infinitely uniform on the third dimension). To further simplify the model, all object surfaces are modeled as perfect electric conductors, hence material losses (other than loss due to diffuse scattering) are not included in this analysis. Besides, to numerically model the surface roughness of all the objects, we use the root mean square height (h) and correlation length (L) to describe the roughness [29]. In this article, we assume that the walls and targets have a h/L of 0.05 mm/0.2 mm and 0.1 mm/0.2mm, respectively, which are close to common building surfaces [28].

To create lines with random roughness based on the desired total length, number of points, h, and L, we first generate random data with distribution and autocovariance functions both being Gaussian, then import them into the numerical 2-D EM solver (WIPL-D 2-D Solver, commercially available [30]) to construct a rough (wiggly) line. We note that the number of points needs to be large enough such that the segment length is smaller than L/2 to fulfill the Nyquist sampling theorem. Also, to achieve adequate Gaussian statistics, the total length of the rough line needs to be much larger than L (> 500 times larger in our model).

For this article, the THz imaging aperture consists of a 161-element linear antenna array with uniform excitation and spacing. The antennas radiate THz waves in the band of 290–300 GHz and coherently detect the backscattered signals. In addition, to avoid grating lobes in the array factor, the spacing between the elements is  $\lambda/2$  at the highest frequency [31], namely 0.5 mm. Thus, the total aperture size is 8 cm. Besides, all the antennas are omnidirectional and linearly polarized (normal to the topology plane).

Fig. 4(a) shows the obtained initial image using a frequency band of 290–300 GHz (the image reconstruction algorithm is introduced in the Appendix). We notice that: two LoS walls are correctly reconstructed (marked in green); both LoS walls generate "ghosts" (marked in yellow) due to the multiple reflections between themselves; and NLoS objects also create "ghosts" (marked in red), the two at the top are resulted from the right-handed wall whereas the one at the bottom is created due to the multiple reflections between the walls. Then, following the image correction process discussed above, we mirror the shadow areas behind the LoS walls [see Fig. 4(b)] to determine the accurate positions and orientations of the NLoS objects. Here, in this example multiple first-generation shadow areas are present, they are independent from each other, and we need to handle them one by one (sequence can be arbitrary). Similarly, if more LoS surfaces are involved, all the resulting first-generation shadow areas would be independent and the processing sequence does not affect the final image. As such, Fig. 4(c)-(e) depict the image correction steps using *mirror folding*. The corrected image, as depicted in Fig. 4(e), agrees with the actual topology of the simulation model (see Fig. 3).

Besides, as we discussed, due to the multiple reflections, a single object (LoS or NLoS) can produce multiple "ghosts" in the raw image [see Fig. 4(a)]. Thus, during the processing of image correction using mirror folding, those "ghosts" will overlap at

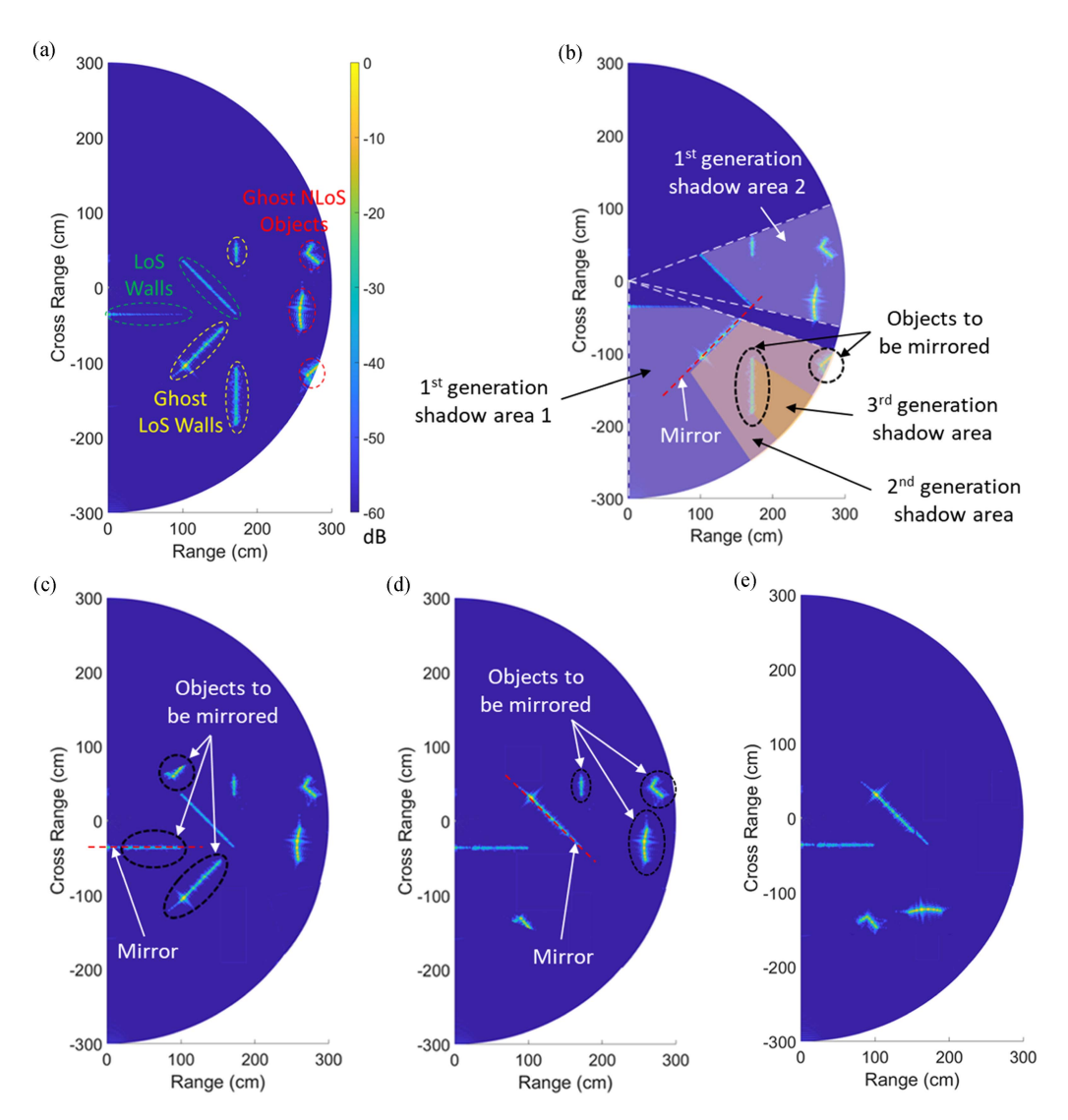


Fig. 4. Simulation of a 2-D THz NLoS imaging scenario (see Fig. 3). (a) Acquired (initial) image depicts several LoS walls as well as multiple "ghost" objects due to multireflection propagation of the THz waves. (b) Pixels are hierarchically classified into mirrors and objects, depending on the number of signal bounces needed to be imaged. LoS mirrors constitute the parents of the pixels located behind them, such that the first NLoS mirror is a first generation mirror. Generations increase with the number of bounces. To properly reconstruct the NLoS scenes, *mirror folding* is applied multiple times beginning from the last generation toward the parent (LoS) mirrors. We notice that the third generation shadow area does not contain any objects. As such, the second generation pixels inside the purple marked area are mirrored around the respective mirror. (c) Then, these mirrored pixels (marked) "age" and move to the previous generation. As a result, they are mirrored again but around the parent mirror. (d) Similarly, the first generation pixels (marked) are mirrored around the second parent (LoS) mirror to finally form (e) the corrected image that recovers the geometries of the original geometry.

some point. In this case, we can simply keep the voxel/pixel with a stronger magnitude to enhance the image's sharpness.

The simulated scenario demonstrates that the proposed THz around-the-corner imaging approach is valid in a scenario where both LoS and NLoS objects are multiple and the multireflection effect is substantial. It also shows that the *mirror folding* method can effectively account for the case of one object being reflected through multiple surfaces. This indicates the proposed method can be potentially applied in a dense and complicated environment with an unknown number of reflections.

### IV. MIRROR FOLDING ALGORITHM

The initial image captured by the imaging aperture (e.g., THz camera) is processed to reveal the correct geometry and

pose of NLoS objects and scenes. We are using an inverse approach to the mirror unfolding approach used in ray tracing methods in computer graphics. We term this approach *mirror folding* and it is given in Table I. After the initial THz image is acquired, the method detects linear segments of minimum length and classifies them as mirrors. The relative position of every mirror determines the number of bounces that the signal has encountered by assuming that surfaces is opaque to the THz waves.

This multibounce propagation is modeled as a hierarchical tree (see Fig. 5) where behind every mirror the subsequent pixels belong to the respective mirror generation tree. The number of generations depends on the number of bounces. Finally, by systematically applying mirror folding, we reconstruct the correct geometry and pose of both LoS and NLoS scenes. Although for

#### 

- 1. Raw image acquisition: The THz camera generates a 3D matrix forming the initial image (cross-range and range). The numerical value assigned to each voxel corresponds to the intensity of the backscattered signals. Additionally, to compensate for the free space path loss, each voxel's intensity is normalized with the  $r^2$  factor (r is distance of voxel from the THz camera's reference point). Besides, to extract a 2-D image (horizontal cross-section) as we demonstrated in this article, we only keep the pixel with the maximum value in every vertical cross-range column.
- 2. Determine the mirror pixels: Set a threshold T such that only the pixels with an intensity >T are considered as objects whereas others are recognized as free space. Then, apply the Hough transform (a computational method of detecting lines in the input image by finding aligned points) on the objects to determine the linear segments that correspond to flat surfaces (mirrors) [32]. The remaining pixels above threshold T are assumed to be non-mirror (objects) and do not contribute to multipath propagation.
- 3. Hierachical mirror classification based on the number of bounces: As shown in the diagram of Fig. 9, the detected flat surfaces in the LoS are designated as the "parent" mirrors (e.g., image.mirror().line()). Accordingly, other identified flat surfaces at longer range distances (i.e., appear to be behind LoS mirrors) become "child" mirrors. For example, for a second bounce mirror the corresponding pixel line will be

image.mirror(i).mirror(k).line()

- where *i* corresponds to the i<sup>th</sup> LoS mirror (first generation) and *k* corresponds to the k<sup>th</sup> next generation mirror of the i<sup>th</sup> LoS mirror. This way, the total number of bounces determines the number of mirror generations.
- 4. *Hierachical (non-mirror) object classification:* After the mirror detection and classification, the remaining pixels above the threshold *T* are classified hierarchically similar to the mirror classification process (step 3), as shown in diagram of Fig. 9. As such, each mirror determines a shadow region with child mirrors and/or non-mirror objects. For example, *image.mirror(1).mirror(3).objects()* stores the indices of the pixels in the shadow area of the 3<sup>rd</sup> child mirror behind the 1<sup>st</sup> LoS mirror.
- 5. Apply mirror folding on every branch of the tree structure:

j = maximum number of bounces

while j > 0

for t < number of mirrors of j<sup>th</sup> bounce

- (i) Rotate all objects around the line defined by the parent mirror (find the new coordinates)
- (ii) Assign the new pixel coordinates to the previous generation. For example, the updated coordinates of *image.mirror(2).mirror(1).objects()* will be stored into the *image.mirror(2).objects()* method.

 $t \leftarrow t+1$  $j \leftarrow j-1$ 

6. Finally, *image.objects()* contains the pixels of the reconstucted scene.

this article the reconstruction has been limited to 2-D images and flat surfaces, it can be easily generalized for 3-D images and curved surfaces.

#### V. VALIDATION OF THZ NLOS IMAGING

To demonstrate THz NLoS imaging, we carried out experiments for various propagation scenarios. Two imaging systems, based on raster scanning and synthetic apertures, are used to investigate 3-D and 2-D NLoS imaging, respectively.

#### A. Material Loss Characterization of Drywall

In the case of THz waves scattering from a rough surface, the scattering loss has two major contributors: diffusion due to surface roughness and material loss due to dielectric constant mismatch between air and the surface and conductivity. In the simulation discussed in Section III, we used PEC to simplify the scenario and hence save computational resource. To understand the total scattering loss in practical applications, we measured both diffuse and specular scattering of a drywall sample. Using the measurement setup we presented in [28] [see Fig. 6(a)], we compare scattering loss between a drywall sample and a smooth (polished) copper plate. Fig. 6(b) shows the measured scattering

pattern when the angle of incidence  $\theta_1=45^\circ$  (normalized to the maximum value of copper plate curve) at 500 GHz. We notice that: both the copper plate and drywall surfaces show a strong specular reflection (angle of reflection  $\theta_2=45^\circ$ ); the drywall sample has stronger diffuse scattering due to surface roughness; and the difference between the two samples at the specular angle is  $\sim\!10$  dB. Therefore, drywall has a moderate round-trip total scattering loss of  $\sim\!20$  dB and can operate as a lossy mirror in the proposed THz NLoS imaging approach.

From our study in [15], the diffuse scattering contributes to the high attenuation noticed in optical NLoS systems. However, here the diffuse scattering component is orders of magnitude weaker than the specular component. In this approach, the diffuse scattering component is mainly used to image the LoS surfaces which are closer to the THz radar. Depending on the dynamic range of the THz imaging system, NLoS imaging with multiple bounces can be achieved, however the number of bounces is now limited by the diffuse scattering losses.

# B. Imaging Experiments Using Raster Scanning

First, we implement a THz NLoS experiment using a 3-D THz radar imaging system, as depicted in Fig. 7(a). The 3-D THz

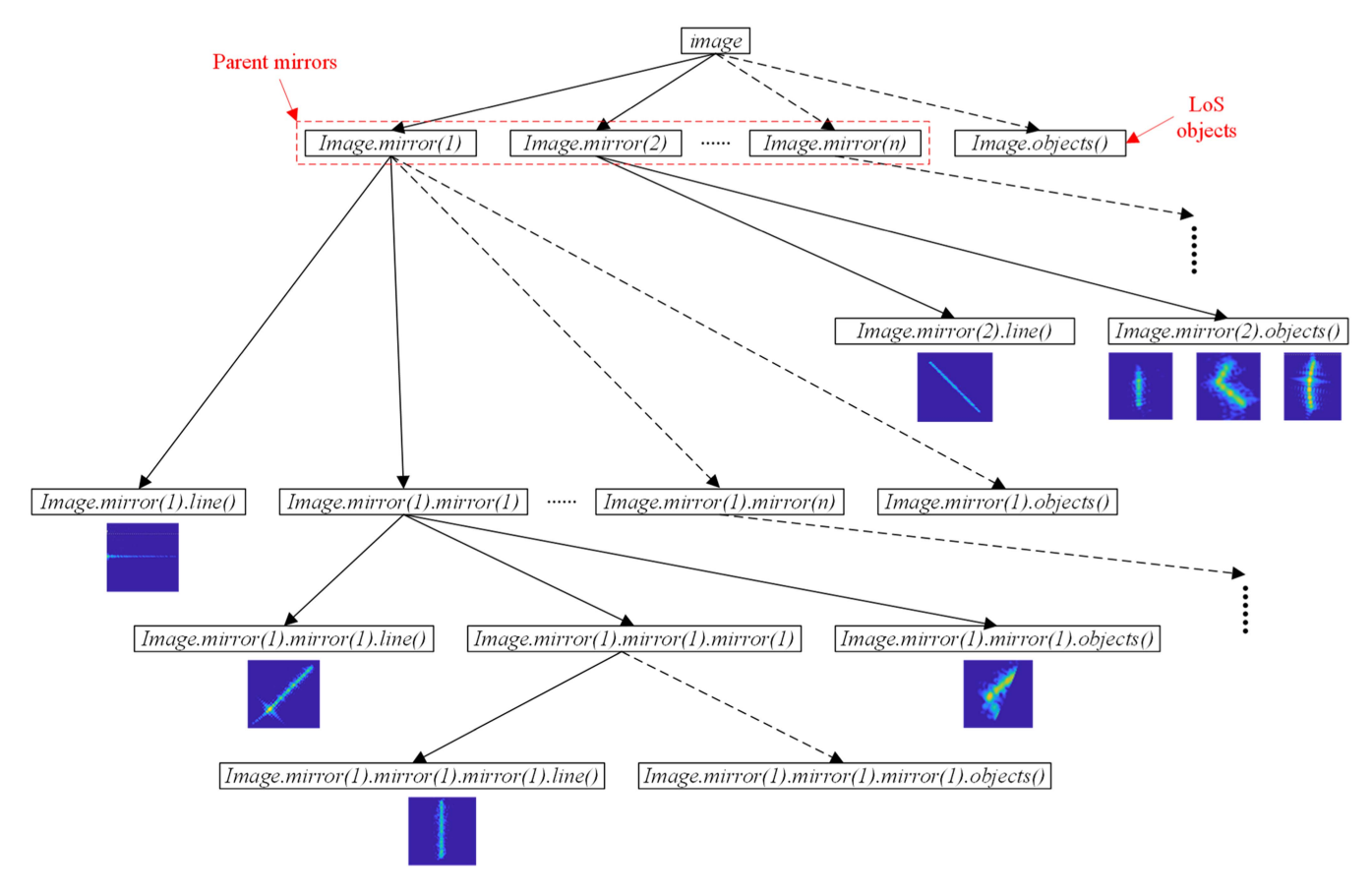


Fig. 5. Tree structure of the hierarchical classification of mirrors and other objects on the initial THz image [see Fig. 4(a)].

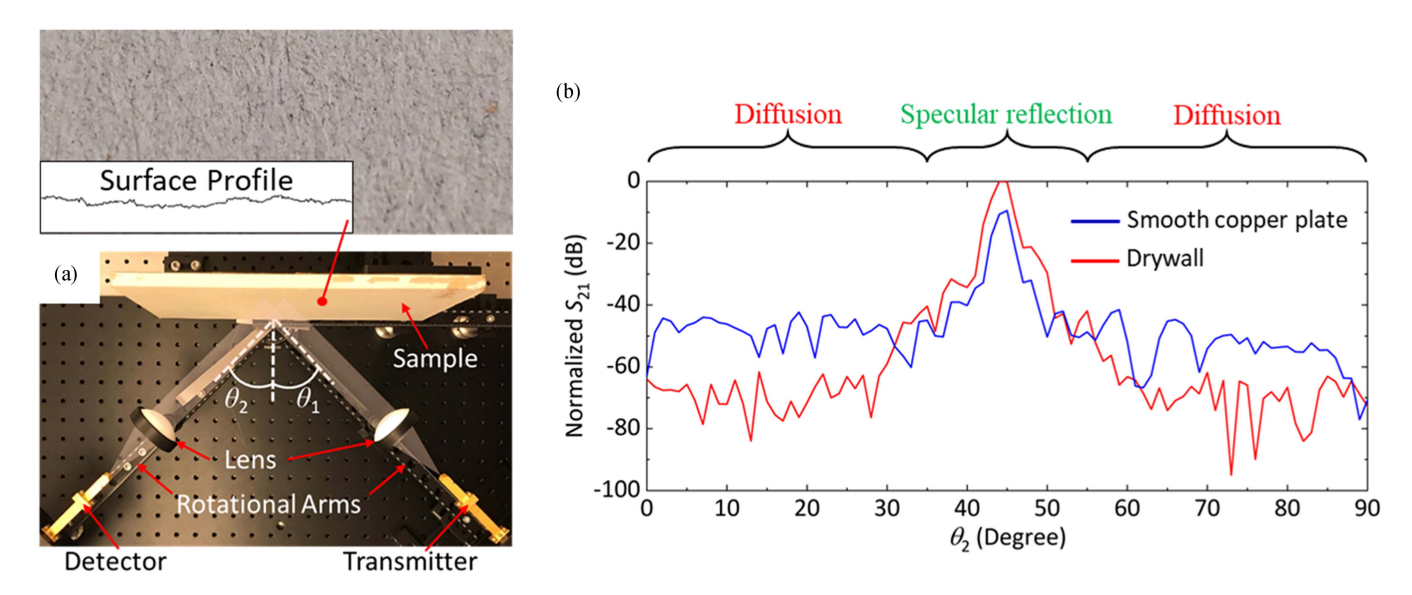


Fig. 6. (a) Measurement setup for the total wave scattering loss characterization. <u>Inset</u>: Close-up picture of the drywall sample and the surface profile obtained using an optical profilometer. The measured roughness parameters for this sample are h = 0.01 mm and L = 0.15 mm. (b) Measured scattering pattern of the drywall sample and a smooth copper plate.

radar system comprises a transceiver integrated with a diagonal horn antenna, a Teflon lens, and a motorized rotational mirror. Here, the transceiver is a vector network analyzer (VNA, model: Rohde & Schwarz ZVA24) extension module (model: Virginia Diodes WR3.4-VNAX) that measures the  $S_{11}$  parameter in

the WR3.4 band (220–330 GHz). The horn has a half-power beamwidth and gain of 10° and 26 dB, respectively. Thus, together they emit a diverging THz beam into the free space. Besides, the customized Teflon lens has a focal length of 44.3 cm so that, when it is placed in front of the horn at a distance of

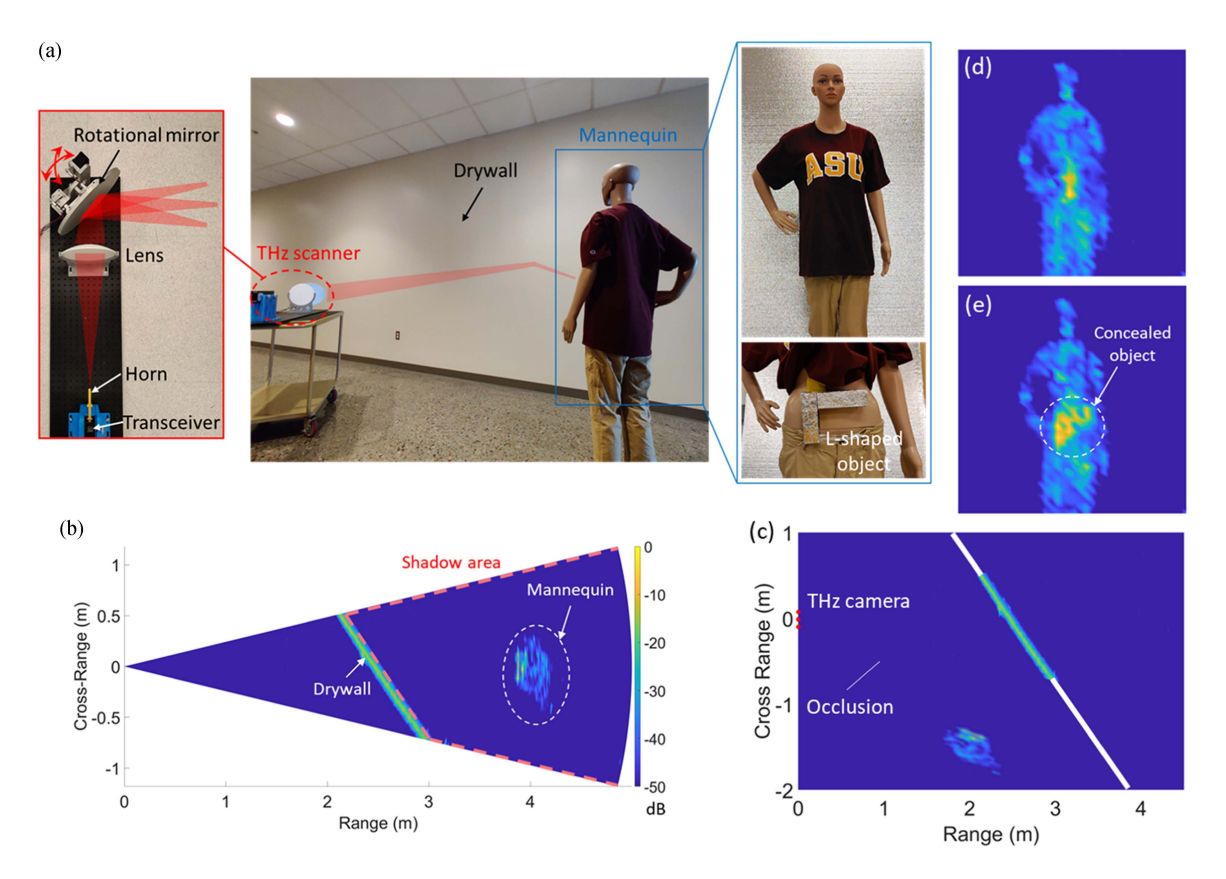


Fig. 7. Concealed object detection in THz NLoS imaging. (a) Measurement setup: a drywall in the LoS is used to image a hidden mannequin (occlusion not included). The mannequin carries a concealed L-shaped metallic object under the shirt. (b) Horizontal cross section of the reconstructed image. The mannequin appears to be behind the drywall. (c) Using *mirror folding*, a correct image that agrees with the actual topology is obtained. (d) and (e) Vertical cross sections before and after removing the concealed object showing the posture of the mannequin.

50 cm, the diverging beam is focused on a spot with a radius of approximately 1.7 cm at a distance of 3.6 m (assuming 300 GHz frequency). Additionally, the customized rotational mirror is driven by two stepper motors to enable controlled rotation in both azimuth and elevation angles. Thus, the lens forms a narrow THz beam while the mirror enables beam steering  $(\pm 15^{\circ})$ .

In the imaging scene, drywall is used as the LoS mirror (more detailed properties of the drywall sample, including the wave scattering measurement results, can be found in [28]), and a life-sized mannequin is placed in the NLoS. The imaging system uses optics (i.e., a lens and a rotational mirror) to generate a narrow THz beam that scans in both azimuth and elevation directions (approximately  $\pm 15^{\circ}$  range). Thus, the scanner stares at the drywall at an oblique angle such that the signals are reflected toward the NLoS scene. As such, using a measurement frequency band of 270-300 GHz, we obtain an initial image (horizontal cross section) as depicted in Fig. 7(b) (the image reconstruction algorithm is discussed in the Appendix). We notice that the drywall is at the expected location and orientation. It appears to be thicker compared with the simulation results because the simulation does not account for the effect of volume scattering that occurs within a shallow depth inside the drywall material [33]. In addition, the shape of the mannequin is present behind the drywall due to the strong specular reflection, however with a wrong pose. In the corrected image obtained using the mirror folding method presented in Fig. 7(c), we notice that it agrees with the actual measurement setup topology. Moreover, a vertical cross section of the mannequin is depicted in Fig. 7(d), showing its outline and posture.

To highlight the relatively low-loss propagation under specular reflection, we present a scenario where the mannequin carries an L-shaped object (covered with aluminum foil to increase the reflectivity) under clothing. As depicted in the vertical cross section of the mannequin [see Fig. 7(e)], we can identify the concealed (i.e., covered by the mannequin's clothing) object appearing as a brighter area due to a stronger backscattering. Therefore, THz NLoS imaging has the potential to reveal concealed objects under clothing, which is beneficial to security applications.

Next, we deploy this 3-D THz radar system to a more complicated NLoS imaging scenario, as shown in Fig. 8(a). The scene comprises the corner of a corridor entrance in the LoS whereas a life-sized mannequin and the inner side of the corridor (with a metallic fire extinguisher box) are in the NLoS. Using a measurement bandwidth of 270–300 GHz, Fig. 8(b) shows a horizontal cross section of the obtained initial image. We observe that: both LoS walls are correctly imaged, including the right angle between them; all the NLoS objects are revealed, including the mannequin, fire extinguisher box, and the NLoS walls; and the NLoS wall appears at ~7 m range is the result of multiple reflections. Besides, the metallic fire extinguisher box exhibits stronger backscattering and hence is brighter in

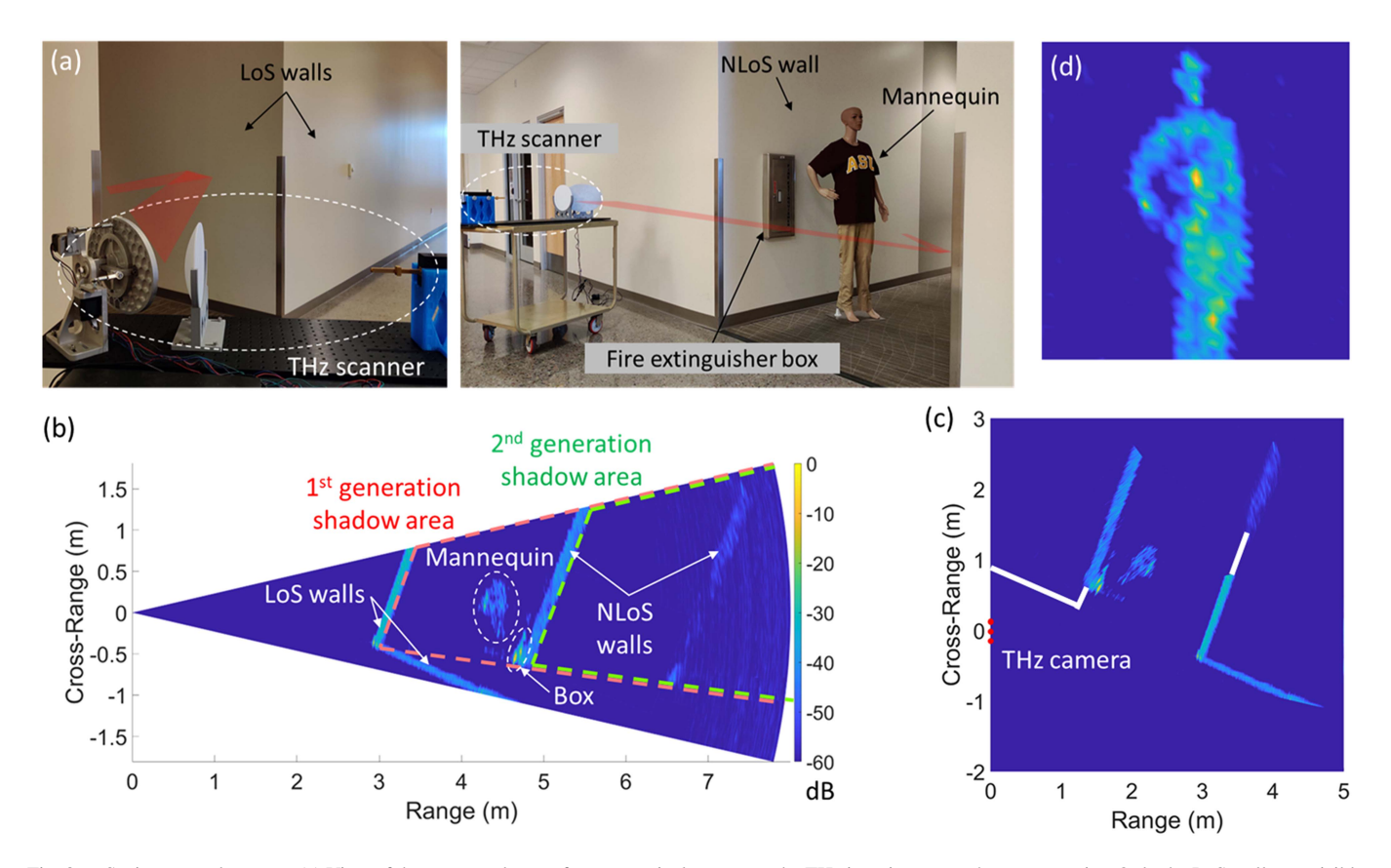


Fig. 8. Seeing around corners. (a) View of the scene under test from an optical camera at the THz imaging system's vantage point: Only the LoS walls are visible whereas a mannequin and other parts of the hallway are in the NLoS. (b) Horizontal cross section of the reconstructed image. The NLoS objects appear to be behind one of the LoS walls. (c) Using *mirror folding*, a correct image that agrees with the actual topology is obtained. (d) Vertical cross section shows the mannequins geometry and pose.

the image. Fig. 8(c) depicts the correct image achieved by applying *mirror folding*. We notice that it properly reflects the actual measurement environment. In addition, Fig. 8(d) shows a vertical cross section of the mannequin; we can easily recognize its outline and posture.

Although the NLoS wall at a further range in Fig. 8(b) appears to be relatively blurred due to the use of a single THz transceiver with a limited SNR ( $\sim$ 50 dB) in the measurement and the energy falloff with the propagation distance increasing, the results prove the effectiveness of the proposed method in solving NLoS imaging problems with multiple reflections. Using a dedicated THz radar imaging system with a stronger output power and a receiver with a higher SNR, we can further improve the imaging range and measurable number of reflections.

# C. Imaging Experiments Using Synthetic Apertures

Nevertheless, to achieve high resolution and long imaging range, large apertures are needed to focus the beam to a small spot with a centimeter-scale size. Therefore, an imaging setup based on optics (e.g., lens and mirror) can be bulky with meterscale optical components [21]. Additionally, the mechanical movement used to implement beam steering (e.g., translation and rotation) is a bottleneck in achieving a subsecond frame rate.

An alternative approach is to use antenna arrays. They can accomplish a fast imaging rate, 3-D image reconstruction, large FoV, and planar structure while maintaining a moderate aperture size to ensure good spatial resolution. To emulate the use of antenna arrays for imaging, we use a synthetic aperture radar (SAR) to evaluate THz NLoS imaging scenarios, as shown in Fig. 9(a). Here, to reduce the image acquisition time, we implemented a linear SAR (2-D imaging), but the approach can be extended to 3-D imaging.

The synthetic aperture imaging system includes a transceiver-receiver pair (instead of using only one transceiver as in the 3-D THz radar) for a better dynamic range. Both of them are VNA extenders in the WR3.4 band and integrated with diagonal horn antennas. The extenders are respectively mounted on two translation stages (model: Thorlabs LTS150/M) such that we translate the transceiver for 81 steps with a spacing of 0.5 mm ( $\lambda$ /2 at the highest frequency). Meanwhile, at each step, the receiver is translated in the same way (81 steps, 0.5 mm spacing) and coherently records the backscattered signals by measuring the  $S_{21}$  parameter. In addition, the extenders are placed as close as possible to minimize the effect of aperture dislocation. As such, we emulate a linear antenna array with full multistatic measurement capability.

In this experiment, similar to the first experiment using the 3-D THz radar, a drywall is used to image the NLoS scene.

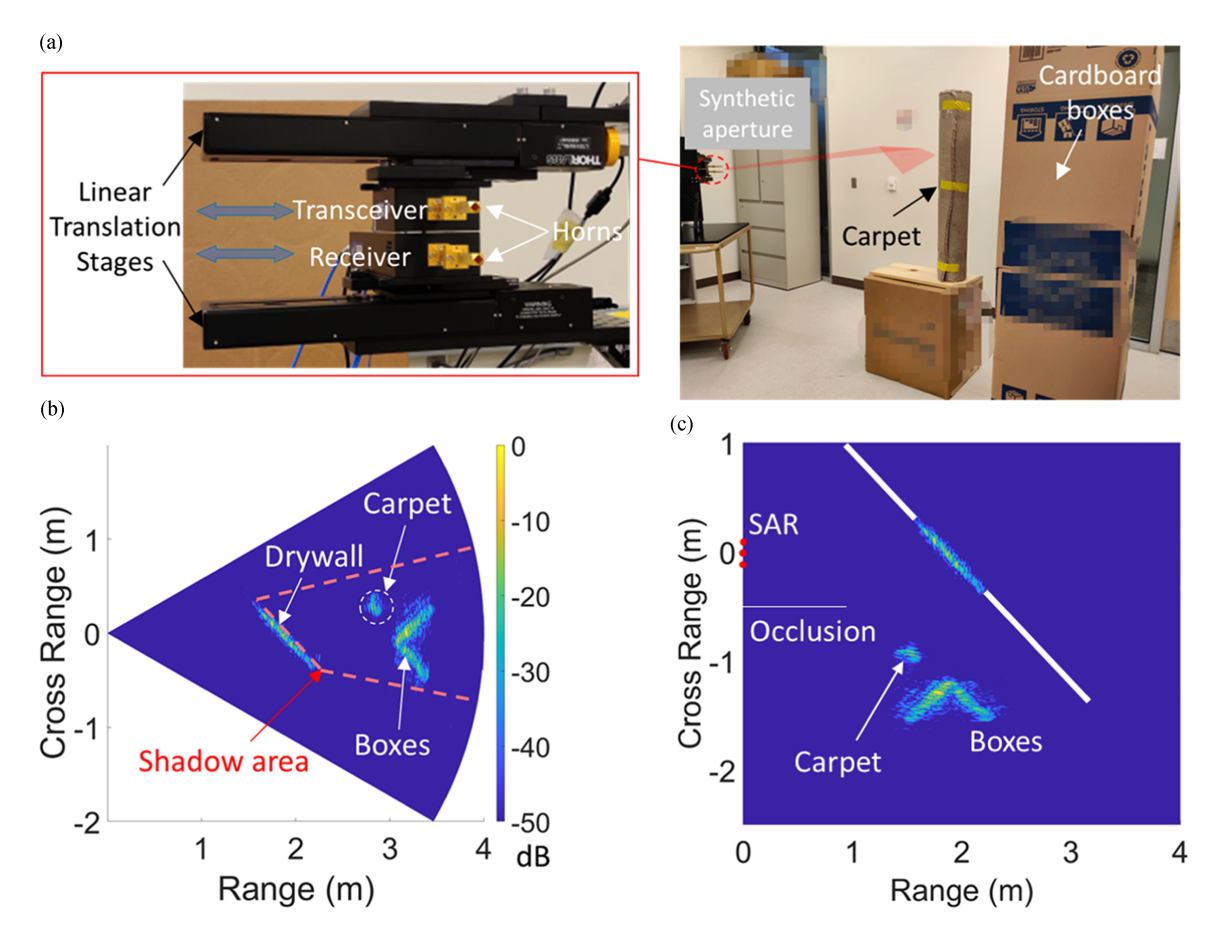


Fig. 9. THz NLoS imaging experiment using synthetic apertures. (a) Picture of the measurement setup where a drywall is used to image the NLoS scene (occlusion not included). The synthetic apertures consist of a transceiver and a receiver that are mounted on two linear translation stages, respectively. To emulate 2-D objects, a carpet and cardboard boxes are used. (b) Initial image shows that the drywall is at the correct location but the NLoS objects appear to be behind it. (c) Correct image is obtained using *mirror folding*.

To fulfill 2-D imaging due to the linear aperture, we use a carpet roll and cardboard boxes (the inner side covered with aluminum foil to block signal penetration) as the NLoS objects. As a result, using a bandwidth of 270–300 GHz, Fig. 9(b) shows the reconstructed image (the image reconstruction algorithm is discussed in the Appendix). We can identify the drywall and two ghost objects in the shadow area. Then, using *mirror folding*, we acquire the corrected image, as depicted in Fig. 9(c). We notice that it agrees with the actual setup topology well. We also note that the box appears to be two relatively straight lines in the image and hence could act as mirrors as well in a more complex scenario. However, in this example, we do not account for that as we do not observe any object within their corresponding shadow areas with a limited dynamic range.

#### VI. DISCUSSION

Although the proposed THz around-the-corner imaging method presents the reconstruction of detailed images containing both LoS and NLoS scenes, more investigation is needed to improve the performance in a broad range of imaging scenarios. For example, arbitrarily shaped objects (nonmirrors) can contribute to the multiple reflection propagation and clutter

the image further. Even if it might be much weaker than the specular reflections of flat surfaces, it can have a deleterious effect with highly reflective materials and with short propagation distances. In other words, even if an NLoS object is classified as a target (e.g., nonmirror surfaces), it could also generate an influential multireflection impact on the image under some conditions. Additionally, if a mirror surface is semitransparent (either due to thin or low-loss material), the objects appearing farther behind will not necessarily be the result of reflection but transmission. Therefore, directly applying mirror folding will result in an erroneous reconstruction of the scene. This could be mitigated by generating images in both vertical and horizontal polarizations which can help distinguish the location of an object with respect to the mirror surface. Furthermore, the mirror folding method can be generalized to account for curved mirror surfaces. This could be achieved by discretizing the curved surface into multiple, smaller planar segments before applying the proposed mirror folding method. Interestingly, the use of convex surfaces can be exploited by THz NLoS imaging to increase the FoV of the system, despite a reduced spatial resolution. Future work could also investigate the efficiency of the imaging method at lower frequencies where surface roughness and spatial resolution (for a given aperture size) become smaller.

This article emphasizes more on the principle and process of the proposed THz around-the-corner imaging method. The image correction algorithm, namely *mirror folding*, has a rather low complexity and can result in video rate NLoS image acquisition when deploying the necessary THz sources and receivers. On the other hand, the selection of a proper mathematical algorithm for the initial image reconstruction from the recorded measurement data is crucial for the overall imaging time.

Prior works have shown that THz wavelengths are long enough to feature a relatively low propagation attenuation than optical bands, especially in the case of fog, smoke, and dust [34]. As such, the proposed method could be used in NLoS situations where optical/infrared visibility is limited. Additionally, THz NLoS imaging systems would be immune to ambient light conditions.

Although we only showed demonstrations with a total range of several meters, the proposed THz imaging method is expected to be valid in a much larger distance (potentially > 20 m) because of the low system loss as estimated in [15]. Additionally, the experiments presented in this article used relatively weak transmitted power (< 0 dBm), thus using stronger THz sources [35] will increase the distance drastically. Meanwhile, the submillimeter scale wavelength of THz signals also enables a high spatial resolution even at a large distance. On the other hand, to achieve a narrow beam spot at a further range, a larger system size is required. For example, for a lens-based wave focusing system (similar to the THz scanner we used in the experiments), a < 3 cm beam spot size can be obtained at a distance of 20 m using a lens diameter of less than 32 cm.

Nevertheless, THz around-the-corner NLoS imaging can provide motivation and impact in other related areas. The requirement for high spatial resolution and bandwidth can be achieved with advances in THz monolithic integrated circuit fabrication and integration techniques, planar antenna arrays, and programmable metasurfaces for electronic beamforming. Additionally, the proposed method can be used to develop physics- and machine learning-based radar algorithms for NLoS imaging, sensing, and detection. In summary, with the development of compact and economical planar THz antenna array structures, using lightweight and robust THz electronics (rather than optical instruments) can promisingly achieve: all-day, high-accuracy, fast-rate, long-time, and heavy-duty around-the-corner NLoS imaging, and a good balance between resolution, cost, and system complexity.

## VII. CONCLUSION

In this article, we propose a method of NLoS (around-the-corner) imaging using THz signals. Common building materials exhibit a very strong specular reflection in the case of THz wave illumination. This lays the foundation for THz around-the-corner imaging as the specular reflection can be used to deflect the signals from the imaging aperture to the invisible scene. However, it also leads to incorrect images as the NLoS objects will appear at the wrong locations. Thus, we introduced a computationally efficient post-processing method (i.e., *mirror* 

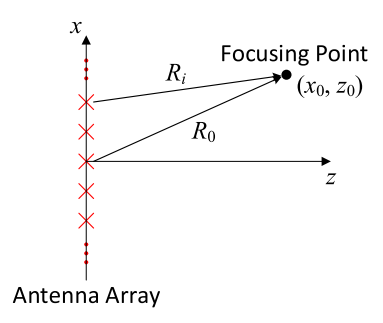


Fig. 10. Illustration of the geometrical relationship between the antenna array and a focal point.

*folding*) to correct the initial images such that the hidden scene can be properly reconstructed.

To demonstrate THz NLoS imaging, we performed 2-D simulations in the 290–300 GHz frequency band. Moreover, we carried out multiple measurements in the range of 270–300 GHz to further validate THz NLoS imaging. Two types of imagers are used: a 3-D radar based on raster scanning and a synthetic aperture imaging system. In various scenarios, we achieved satisfying imaging results with centimeter-scale resolution. The experiments also showed that multibounce wave propagation in the NLoS area can be accounted for in the proposed approach.

#### **APPENDIX**

The 2-D simulation and the synthetic aperture imaging method have the same image reconstruction algorithm. We treat the transmitting (Tx) and receiving (Rx) linear arrays as a MIMO system such that they record the backscattered signals for all the Tx-Rx combinations. To generalize the method to cases where imaging aperture sizes are comparable to the distance from the region of interest (RoI), we account for the curvature of the wavefront. Thus we use the total focusing method (TFM) [36] which exploits the information of every Tx-Rx pair in the imaging array. In contrast to ultrasound imaging, where TFM is used with pulsed signals, the examples presented in this article assume stepped frequency continuous wave systems. As such, the measurement results form a three-dimensional  $M \times N_{Tx} \times N_{Rx}$  matrix (S), where M is the number of frequency points and  $N_{Tx}$ ,  $R_{Tx}$  are the number of Tx and Rx antennas, respectively.

As depicted in Fig. 10, to form a focused illumination at a point  $(x_0, z_0)$ , we consider the distance between the focusing point and each antenna element independently. Thereby, the relative phase delay of the signal at the *i*th antenna on the array is

$$\varphi_i = \frac{2\pi}{\lambda} \ (R_i - R_0) \tag{1}$$

with

$$R_0 = \sqrt{{x_0}^2 + z_0^2} \tag{2}$$

$$R_i = \sqrt{(x_i - x_0)^2 + z_0^2} \tag{3}$$

where  $\lambda$  is the wavelength,  $R_0$  and  $R_i$  are the distances of the focusing point from the array center (reference element, zero phase) and the *i*th element, respectively. Thus, based on M

frequency points, we acquire two phase matrices  $\Phi_{Tx}$  and  $\Phi_{Rx}$ , with a size of  $M \times N_{Tx}$  and  $M \times N_{Rx}$ , for the Tx and Rx arrays, respectively. The columns of the matrices represent the phase delays of the corresponding elements at every frequency. Then, beam focusing by the Tx and Rx arrays is achieved by applying the necessary phase delays

$$S_0 = \sum_{\text{Dim}_2} \left( \sum_{\text{Dim}_2} S_k \circ \Phi_{\text{Tx}} \right) \circ \Phi_{Rx}.$$
 (4)

Here, the operator  $\circ$  stands for the Hadamard product and  $S_k$  is the kth 2-D matrix along the third dimension of S ( $k=1,2,\ldots,N_{Rx}$ ). Also,  $Dim_2$  denotes that the summation is operated in the second dimension of the matrix. As a result, we obtain a frequency domain vector  $S_0$  with M elements. By applying the inverse Fourier transform (IFT), we acquire the time domain signal:

$$S_t = \text{IFT} \left[ S_0 \circ a \right]. \tag{5}$$

To achieve lower side lobes in the range direction, we taper  $S_0$  before calculating the IFT. For simplicity and without loss of generality, we use the triangular function a, as determined by

$$a[n] = 1 - \frac{2}{M-1} \left| n - \frac{M+1}{2} \right|.$$
 (6)

The time domain vector  $S_t$  is then converted to distance (range) based on the wave velocity in free space  $(c_0)$ . According to the sampling theorem, the maximum unambiguous detectable range is  $c_0/(2\Delta f)$ , where  $\Delta f$  is the frequency step. However, since  $S_t$  is calculated for a single focusing point, we only keep the value that corresponds to the range of this point in  $S_t$ . Finally, following the same process, we calculate the backscattered signal from every focusing point (x, z) in the RoI and combine them to form the reconstructed image.

On the other hand, the 3-D THz radar has a simpler image reconstruction algorithm. At each scanning angle, the transceiver measures the  $S_{11}$  parameter in the frequency domain. Then we convert it to time-domain using the IFT, thus acquiring the range information based on  $c_0$ . As a result, the radar system produces a 3-D matrix with a size of  $N_a \times N_e \times M$ , where  $N_a$  and  $N_e$  are the number of scanning angles in the azimuth and elevation planes, respectively, and M is the number of frequency points (i.e., discretized points along the range direction). Therefore, each matrix element corresponds to a voxel and a 3-D image is obtained by plotting the magnitude of all the voxels.

### REFERENCES

- M. Dehmollaian and K. Sarabandi, "Refocusing through building walls using synthetic aperture radar," *IEEE Trans. Geosci. Remote Sens.*, vol. 46, no. 6, pp. 1589–1599, Jun. 2008, doi: 10.1109/TGRS.2008.916212.
- [2] K. Chetty, G. E. Smith, and K. Woodbridge, "Through-the-wall sensing of personnel using passive bistatic WiFi radar at standoff distances," *IEEE Trans. Geosci. Remote Sens.*, vol. 50, no. 4, pp. 1218–1226, Apr. 2012, doi: 10.1109/TGRS.2011.2164411.
- [3] T. Li, L. Fan, M. Zhao, Y. Liu, and D. Katabi, "Making the invisible visible: Action recognition through walls and occlusions," in *Proc. IEEE/CVF Int. Conf. Comput. Vis.*, 2019, pp. 872–881, doi: 10.1109/ICCV.2019.00096.
- [4] R. Zetik, M. Eschrich, S. Jovanoska, and R. S. Thoma, "Looking behind a corner using multipath-exploiting UWB radar," *IEEE Trans. Aerosp. Electron. Syst.*, vol. 51, no. 3, pp. 1916–1926, Jul. 2015.

- [5] N. Scheiner et al., "Seeing around street corners: Non-line-of-sight detection and tracking in-the-wild using doppler radar," in *Proc. IEEE/CVF Conf. Comput. Vis. Pattern Recognit.*, 2020, pp. 2065–2074, doi: 10.1109/CVPR42600.2020.00214.
- [6] A. Sume et al., "Radar detection of moving targets behind corners," *IEEE Trans. Geosci. Remote Sens.*, vol. 49, no. 6, pp. 2259–2267, Jun. 2011.
- [7] A. Velten et al., "Recovering three-dimensional shape around a corner using ultrafast time-of-flight imaging," *Nature Commun.*, vol. 3, no. 1, Jan. 2012. Art. no. 745.
- [8] G. Gariepy et al., "Detection and tracking of moving objects hidden from view," *Nature Photon.*, vol. 10, pp. 23–26, 2016.
- [9] M. O'Toole, D. B. Lindell, and G. Wetzstein, "Confocal non-line-of-sight imaging based on the light-cone transform," *Nature*, vol. 555, no. 7696, pp. 338–341, Mar. 2018.
- [10] X. Liu et al., "Non-line-of-sight imaging using phasor-field virtual wave optics," *Nature*, vol. 572, no. 7771, pp. 620–623, Aug. 2019.
- [11] R. Cao, F. Goumoens, B. Blochet, J. Xu, and C. Yang, "High-resolution non-line-of-sight imaging employing active focusing," *Nature Photon.*, vol. 16, pp. 462–468, 2022.
- [12] J. H. Nam et al., "Low-latency time-of-flight non-line-of-sight imaging at 5 frames per second," *Nature Commun.*, vol. 12, no. 1, Dec. 2021, Art. no. 6526.
- [13] D. Royo et al., "Virtual mirrors: Non-line-of-sight imaging beyond the third bounce," ACM Trans. Graph., vol. 42, no. 4, pp. 1–15, 2023.
- [14] C. Wu et al., "Non–line-of-sight imaging over 1.43 km," *Proc. Nat. Acad. Sci.*, vol. 118, no. 10, 2021, Art. no. 2024468118.
- [15] Y. Cui and G. C. Trichopoulos, "Comparison of propagation losses in THz and optical non-line-of-sight imaging," in *Proc. IEEE Int. Symp. Antennas Propag. USNC-URSI Radio Sci. Meeting*, 2019, pp. 1473–1474.
- [16] D. B. Lindell, G. Wetzstein, and V. Koltun, "Acoustic non-line-of-sight imaging," in *Proc. IEEE/CVF Conf. Comput. Vis. Pattern Recognit.*, 2019, pp. 6773–6782.
- [17] C. Jansen et al., "Diffuse scattering from rough surfaces in THz communication channels," *IEEE Trans. Terahertz Sci. Technol.*, vol. 1, no. 2, pp. 462–472, Nov. 2011, doi: 10.1109/TTHZ.2011.2153610.
- [18] E. N. Grossman, T. Sasaki, and J. R. Leger, "Passive terahertz non-line-of-sight imaging," *IEEE Trans. Terahertz Sci. Technol.*, vol. 12, no. 5, pp. 489–498, Sep. 2022.
- [19] S. K. Doddalla and G. C. Trichopoulos, "Non-line of sight terahertz imaging from a single viewpoint," in *Proc. IEEE/MTT-S Int. Microw.* Symp., 2018, pp. 1527–1529.
- [20] G. C. Trichopoulos, H. L. Mosbacker, D. Burdette, and K. Sertel, "A broad-band focal plane array camera for real-time THz imaging applications," *IEEE Trans. Antennas Propag.*, vol. 61, no. 4, pp. 1733–1740, Apr. 2013, doi: 10.1109/TAP.2013.2242829.
- [21] K. B. Cooper et al., "THz imaging radar for standoff personnel screening," IEEE Trans. Terahertz Sci. Technol., vol. 1, no. 1, pp. 169–182, Sep. 2011, doi: 10.1109/TTHZ.2011.2159556.
- [22] D. M. Sheen, D. L. McMakin, and T. E. Hall, "Three-dimensional millimeter-wave imaging for concealed weapon detection," *IEEE Trans. Microw. Theory Techn.*, vol. 49, no. 9, pp. 1581–1592, Sep. 2001, doi: 10.1109/22.942570.
- [23] M. Aladsani, A. Alkhateeb, and G. C. Trichopoulos, "Leveraging mmWave imaging and communications for simultaneous localization and mapping," in *Proc. IEEE Int. Conf. Acoust., Speech Signal Process.*, 2019, pp. 4539–4543, doi: 10.1109/ICASSP.2019.8682741.
- [24] B. G. Kashyap, P. C. Theofanopoulos, Y. Cui, and G. C. Trichopoulos, "Mitigating quantization lobes in mmWave low-bit reconfigurable reflective surfaces," *IEEE Open J. Antennas Propag.*, vol. 1, pp. 604–614, 2020, doi: 10.1109/OJAP.2020.3034049.
- [25] R. G. Baraniuk, "Compressive sensing [lecture notes]," *IEEE Signal Process. Mag.*, vol. 24, no. 4, pp. 118–121, Jul. 2007, doi: 10.1109/MSP. 2007.4286571.
- [26] M. Grzegorzek, C. Theobalt, R. Koch, and A. Kolb, *Time-of-Flight and Depth Imaging: Sensors, Algorithms and Applications*, 1st ed. Berlin, Germany: Springer, 2013.
- [27] O. Gupta, T. Willwacher, A. Velten, A. Veeraraghavan, and R. Raskar, "Reconstruction of hidden 3D shapes using diffuse reflections," *Opt. Exp.*, vol. 20, pp. 19096–19108, 2012.
- [28] Y. Cui, M. K. Immadisetty, and G. C. Trichopoulos, "Evaluating the properties of millimeter- and THz wave scattering from common rough surfaces," in *Proc. IEEE Int. Symp. Antennas Propag. North Amer. Radio* Sci. Meeting, 2020, pp. 1117–1118.
- [29] P. Beckmann and A. Spizzichino, The Scattering of Electromagnetic Waves from Rough Surfaces. Norwood, MA, USA: Artech House, 1987.

- [30] WIPL-D 2D Solver v6.0, WIPL-D d.o.o., 2020. [Online]. Available: https://wipl-d.com/products/wipl-d-2d-solver/
- [31] C. A. Balanis, Antenna Theory: Analysis and Design, 4th ed. Hoboken, NJ, USA: Wiley, 2016.
- [32] R. O. Duda and P. E. Hart, "Use of the hough transformation to detect lines and curves in pictures," *Commun. ACM*, vol. 15, no. 1, pp. 11–15, Jan. 1972.
- [33] M. Khatun, C. Guo, D. Matolak, and H. Mehrpouyan, "Indoor and outdoor penetration loss measurements at 73 and 81 GHz," in *Proc. IEEE Glob. Commun. Conf.*, 2019, pp. 1–5, doi: 10.1109/GLOBECOM38437.2019. 9013945.
- [34] K. Su, L. Moeller, R. B. Barat, and J. F. Federici, "Experimental comparison of terahertz and infrared data signal attenuation in dust clouds," *J. Opt. Soc. Amer. A*, vol. 29, no. 11, pp. 2360–2366, 2012.
- [35] J. Hesler, P. Rohit, and T. Jerome, "Advances in terahertz solid-state physics and devices," J. Appl. Phys., vol. 126, no. 11, pp. 1–2, 2019.
- [36] C. Holmes, B. Drinkwater, and P. Wilcox, "The post-processing of ultrasonic array data using the total focusing method," *Insight Non-Destructive Testing Condition Monit.*, vol. 46, no. 11, pp. 677–680, Nov. 2004.



Yiran Cui received the B.E. degree in electronic information engineering from Anhui Normal University, Wuhu, Anhui, China, in 2012, the M.S. degree in electromagnetic field and microwave technology from University of Electronic Science and Technology of China, Chengdu, Sichuan, China, in 2015, and the Ph.D. degree in electrical engineering from Arizona State University, Tempe, AZ, USA, in 2022.

His research interests include mmW/THz measurements, quasi-optical techniques, and mmW/THz imaging systems and applications.



Georgios (George) C. Trichopoulos (Member, IEEE) received the Diploma degree in electrical and computer engineering from the Democritus University of Thrace, Xanthi, Greece, in 2004, the M.S. degree in biomedical engineering from the National Technical University of Athens, Athens, and University of Patras, Patras, Greece (under a joint program), in 2007, and the Ph.D. degree in electrical and computer engineering from the Ohio State University, Columbus, OH, USA, in 2013.

His doctoral work provided fundamental knowledge for the design of real-time terahertz cameras and non-contact probing of mmWave/THz circuits and devices. From 2013 to 2015, he was a Post-doctoral Researcher and a Research Scientist with the ElectroScience Laboratory, Ohio State University. In 2015, he was with Arizona State University, where he is currently an Associate Professor with the School of Electrical, Computer, and Energy Engineering. His research interests include in antennas, microwave engineering, and electromagnetic theory. He focuses on mmWave/THz imaging methods and systems, antenna design for mmWave/THz sensors, and reconfigurable metasurfaces.

Dr. Trichopoulos was the recipient of the Best Student Paper Award in the 2013 IEEE Antennas and Propagation Symposium, Orlando, FL, and the NSF CAREER Award in 2019.